Electronic Supplementary Information (ESI)

Synchronous Immobilization and Conversion of Polysulfides on VO_2-VN Binary Host Targeting High Sulfur Loading Li–S Batteries

Yingze Song,[a†] Wen Zhao,[b†] Long Kong,[c] Li Zhang,*[a] Xingyu Zhu,[a] Yuanlong Shao,[d] Feng Ding,[b] Qiang Zhang,*[c] Jingyu Sun,*[a] and Zhongfan Liu[ae]

[a]*Soochow Institute for Energy and Materials InnovationS (SIEMIS), Key Laboratory of Advanced Carbon Materials and Wearable Energy Technologies of Jiangsu Province, Soochow University, Suzhou 215006, China.*

[b]*Center for Multidimensional Carbon Materials (CMCM), Institute for Basic Science (IBS), Ulsan 689-798, Republic of Korea.*

[c]*Department of Chemical Engineering, Tsinghua University, Beijing 100084, China.*

[d]*Cambridge Graphene Centre, University of Cambridge, Cambridge, CB3 0FA, United Kingdom.*

[e]*Center for Nanochemistry (CNC), College of Chemistry and Molecular Engineering, Peking University, Beijing 100871, China.*

*Corresponding author: sunjy86@suda.edu.cn (J. Y. Sun); zhang-qiang@mails.tsinghua.edu.cn (Q. Zhang); zhangli81@suda.edu.cn (L. Zhang)

†These authors contributed equally to this work.

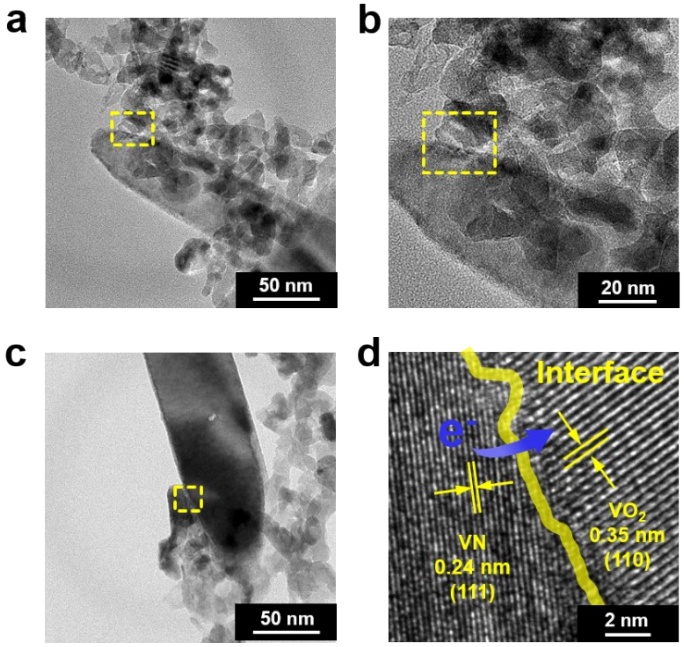

Fig. S1 TEM characterization of VO_2-VN binary host. (a-c) Low-magnified TEM views with the yellow boxes highlighting the interface between VO_2 and VN. (d) High-resolution TEM image disclosing the interface of VO_2-VN.

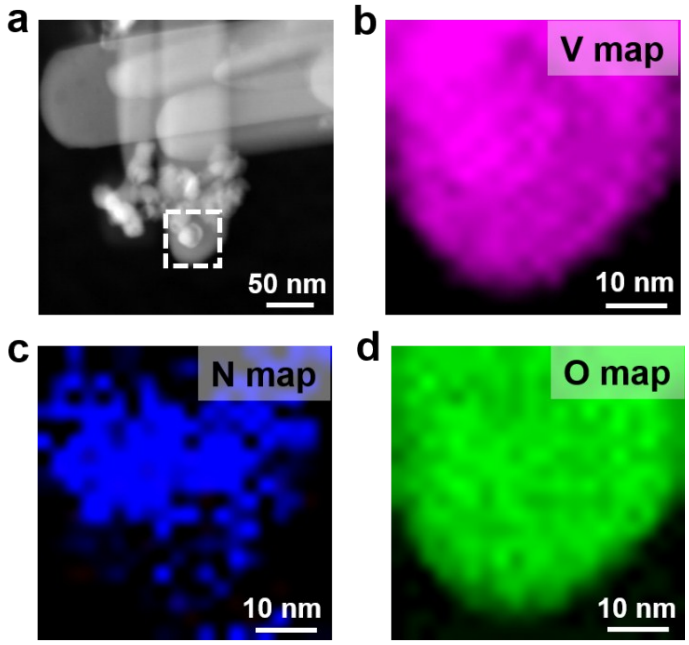

Fig. S2 STEM-EDS characterization of VO_2-VN. (a) STEM image of VO_2-VN, with the marked area probed by EDS. (b-d) Corresponding elemental mapping of VO_2-VN.

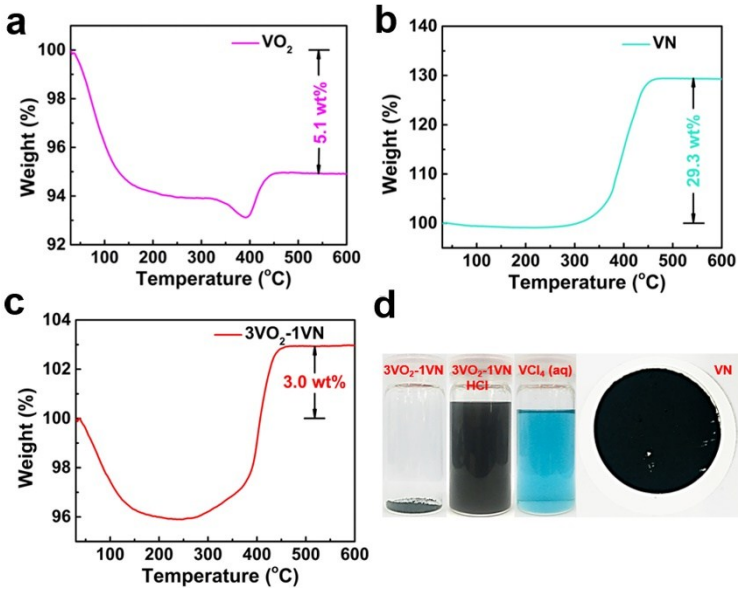

Fig. S3 Experimental determination of exact content of VN within the VO_2-VN hybrid (using $3VO_2$-1VN as an example, with the theoretical VN content of 25 wt%). (a-c) TGA curves of (a) VO_2, (b) VN, and (c) $3VO_2$-1VN. (d) Digital photograph showing the VO_2 dissolution test by HCl acid treatment. From the TGA measurement, the exact content of VN is determined to be ~24 wt%; As for the dissolution test result, the actual VN content is ~23.4 wt%. Both tests confirm the successful fabrication of $3VO_2$-1VN hybrid.

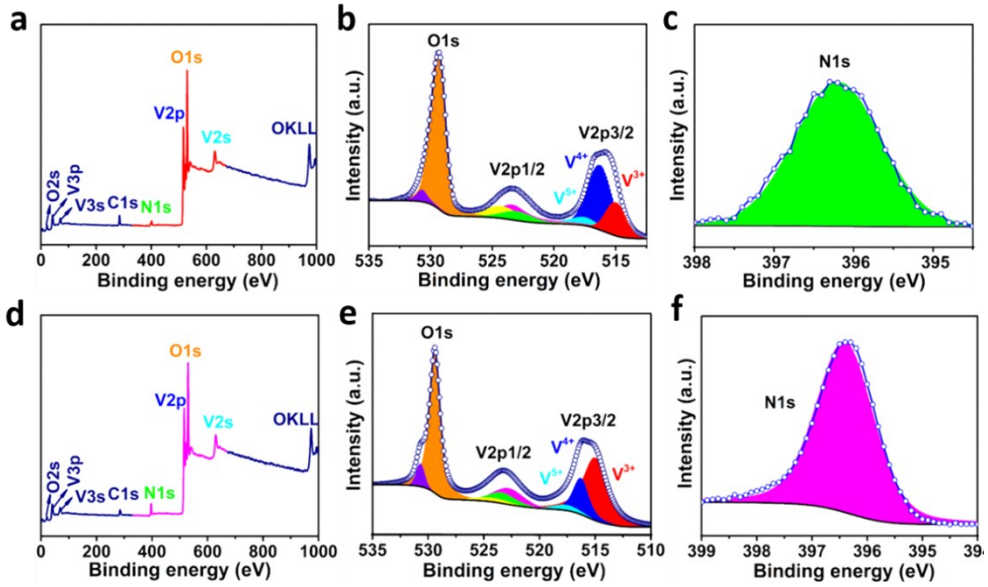

Fig. S4 XPS analysis of (a-c) $3VO_2$-1VN and (d-f) $1VO_2$-3VN binary hosts.

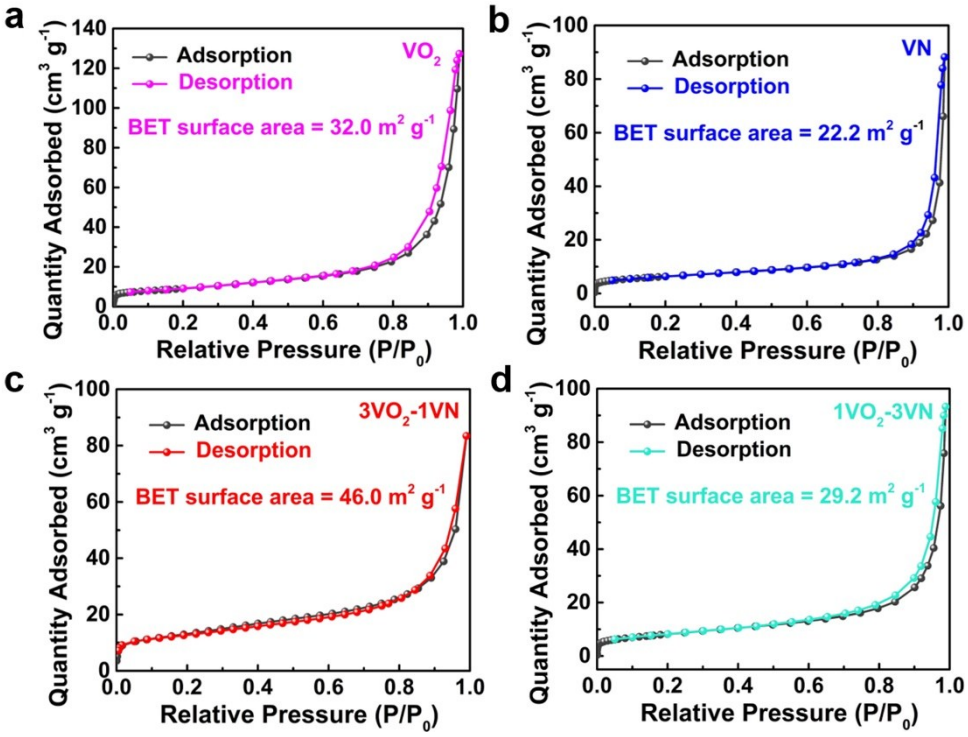

Fig. S5 N_2 adsorption/desorption isotherms of (a) VO_2, (b) VN, (c) $3VO_2$-1VN, and (d) $1VO_2$-3VN. The derived BET surface area value is displayed in each panel, respectively.

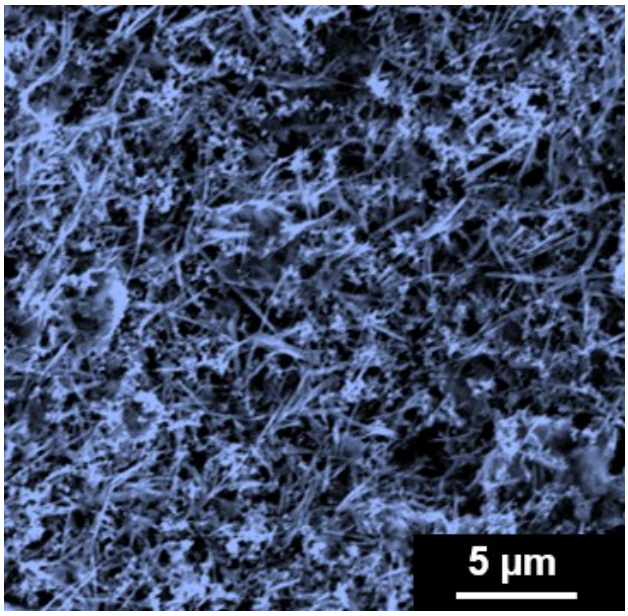

Fig. S6 SEM image of S@$3VO_2$-1VN/G cathode before cycling.

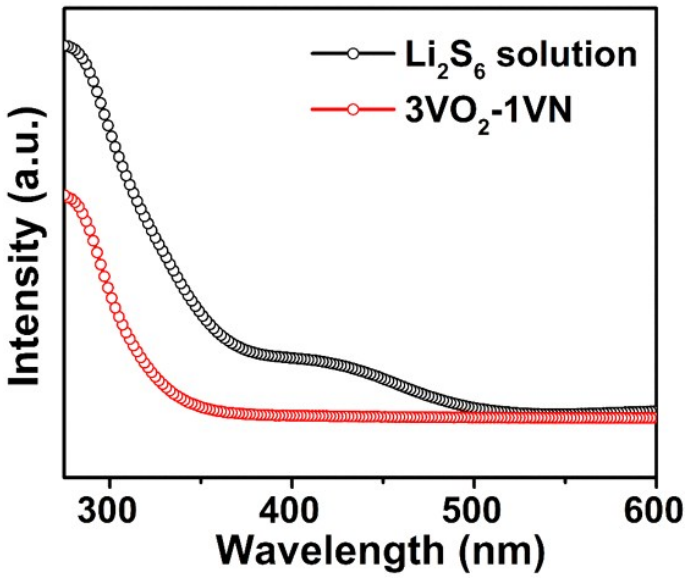

Fig. S7 UV-Vis absorption spectra of a Li_2S_6 solution prior to and after adding $3VO_2$-1VN binary host for 60 s.

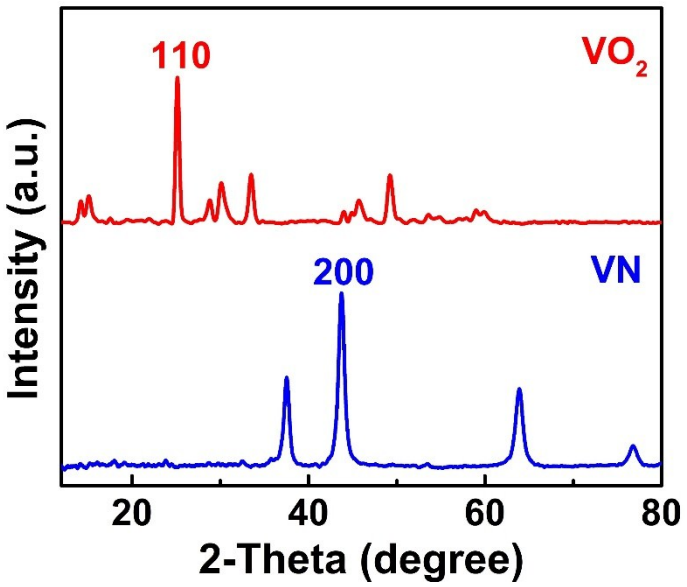

Fig. S8 XRD patterns for as-prepared VO_2 and VN, indicative of dominating and stable facet of VO_2 (110) and VN (200) facets.

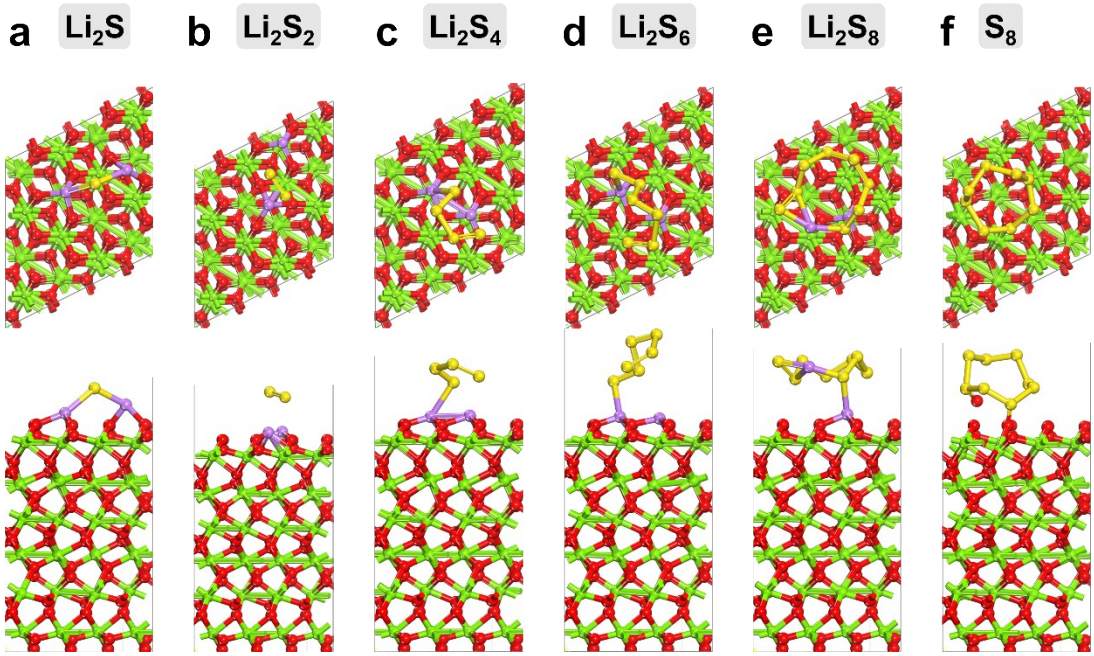

Fig. S9 Optimal configurations of lithium polysulfide Li_2S_x (x =1, 2, 4, 6, and 8) and S_8 clusters adsorbed on the VO_2 (110) surface.

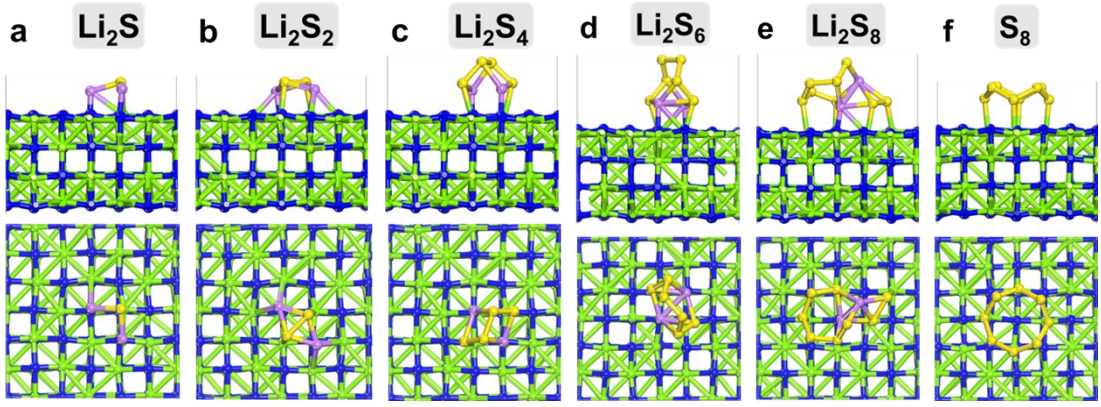

Fig. S10 Optimal configurations of lithium polysulfide Li_2S_x (x =1, 2, 4, 6, and 8) and S_8 clusters adsorbed on the VN (200) surface.

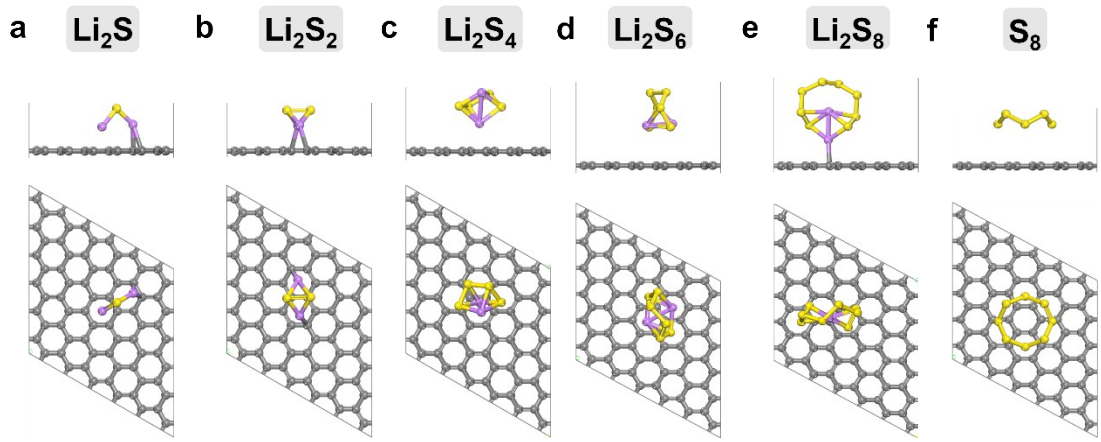

Fig. S11 Optimal configurations of lithium polysulfide Li_2S_x (x =1, 2, 4, 6, and 8) and S_8 clusters adsorbed on the graphene surface.

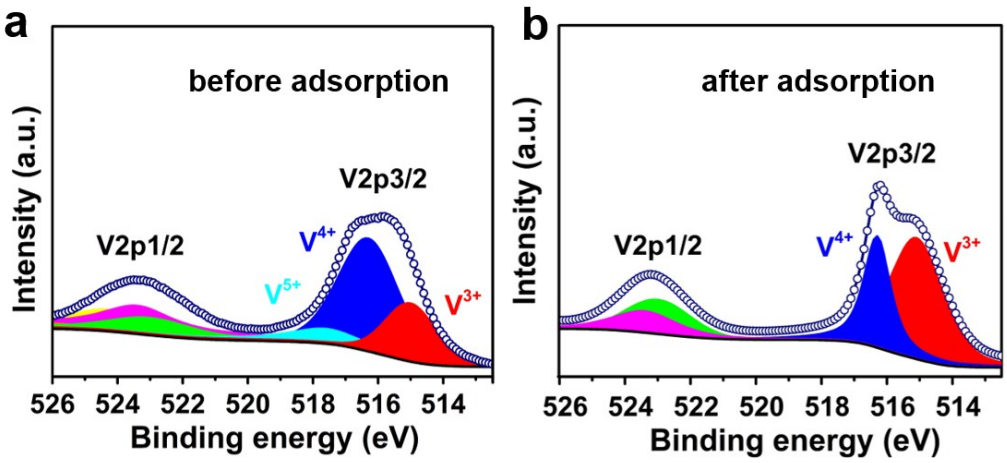

Fig. S12 XPS V2p spectrum of $3VO_2$-1VN (a) before and (b) after Li_2S_6 adsorption showing an obvious change in the valence states for vanadium.

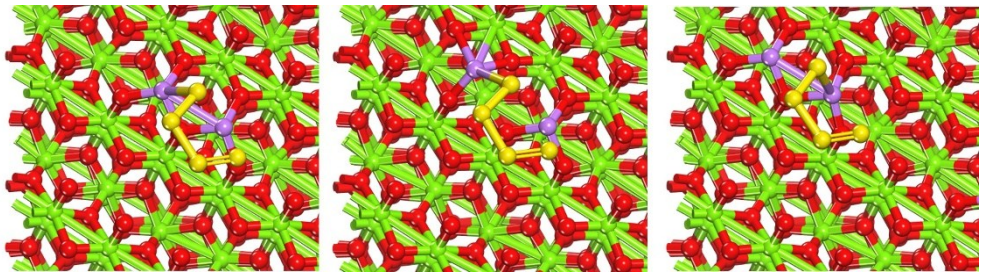

Fig. S13 Top view representations of Li_2S_4 cluster diffusion pathways on VO_2 (110) surface.

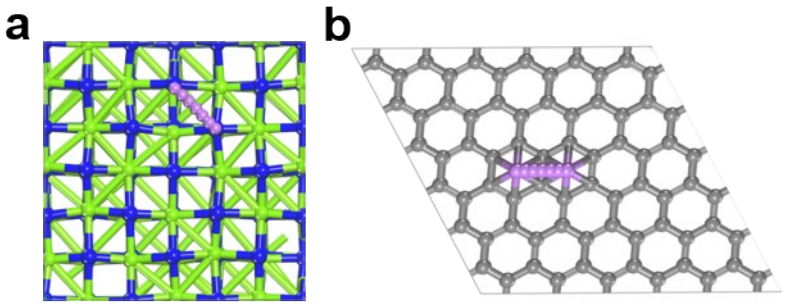

Fig. S14 Top view representations of Li^+ ion diffusion pathways on (a) VN (200) and (b) graphene surfaces.

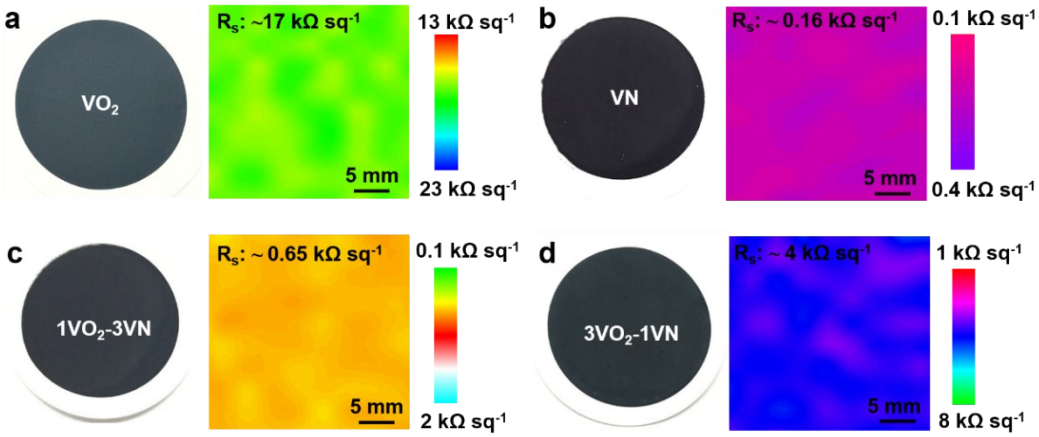

Fig. S15 Digital photographs and corresponding spatial maps of sheet resistances of various material-based films. Each plot of sheet resistance distributions was collected from 100 data points. (a) VO_2, (b) VN, (c) $1VO_2$-3VN, and (d) $3VO_2$-1VN.

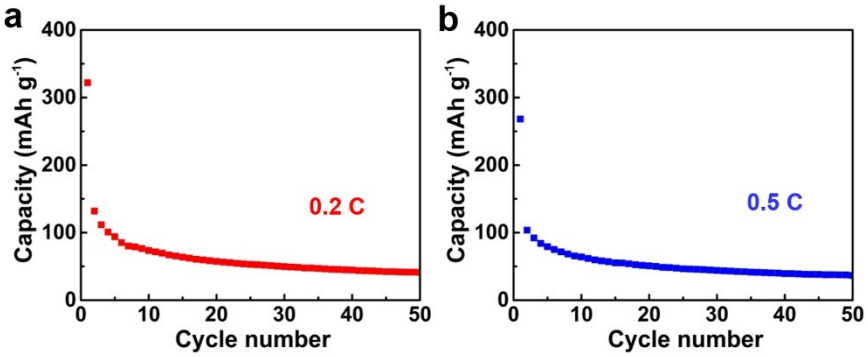

Fig. S16 Cycling performance of bare $3VO_2$-1VN at different current densities.

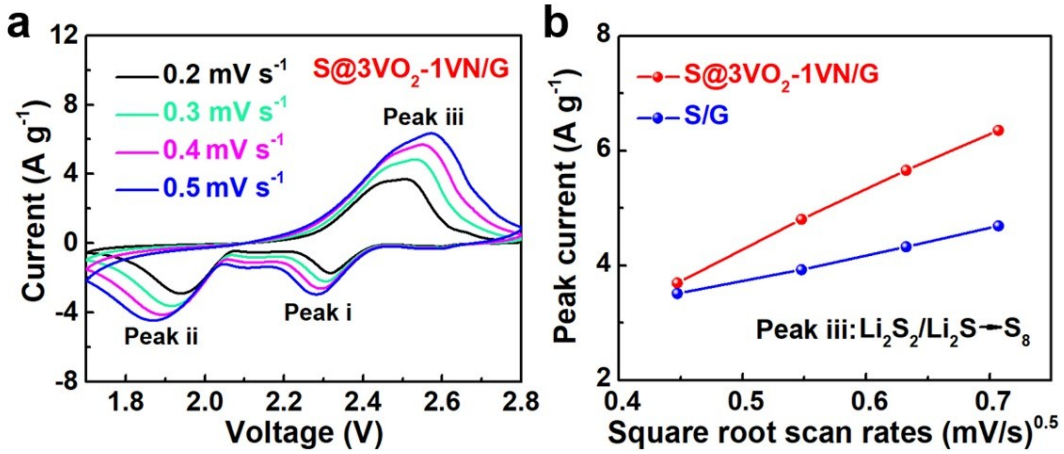

Fig. S17 Investigation of reaction kinetics with respect to catalyzing the oxidation process by $3VO_2$-1VN binary host. (a) CV profiles of S@$3VO_2$-1VN/G cathodes at different scan rates. (b) Plots of CV peak current for anodic oxidation process (Peak iii: Li_2S_2/Li_2S to S_8) *vs.* the square root of the scan rates for S@$3VO_2$-1VN/G and S@G cathodes. Apparently, S@$3VO_2$-1VN/G cathodes demonstrate better oxidation reaction kinetics as compared with that of bare S@G cathodes.

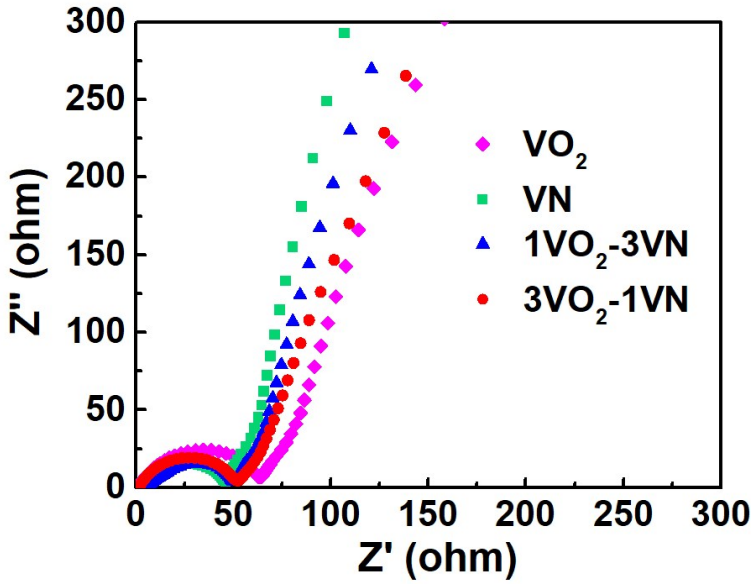

Fig. S18 EIS curves of S@VO_2/G, S@VN/G, S@$1VO_2$-3VN/G, and S@$3VO_2$-1VN/G cathodes.

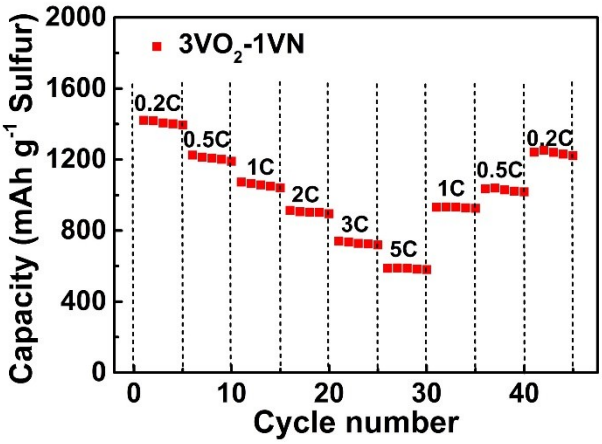

Fig. S19 Rate performance of S@3VO_2-1VN/G cathode at higher current densities of 3 C and 5 C.

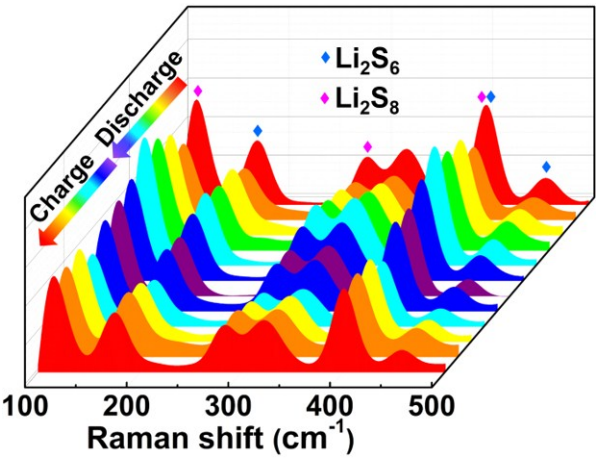

Fig. S20 *In operando* Raman spectra based on bare S@G cathode collected upon the first cycle at 0.2 C.

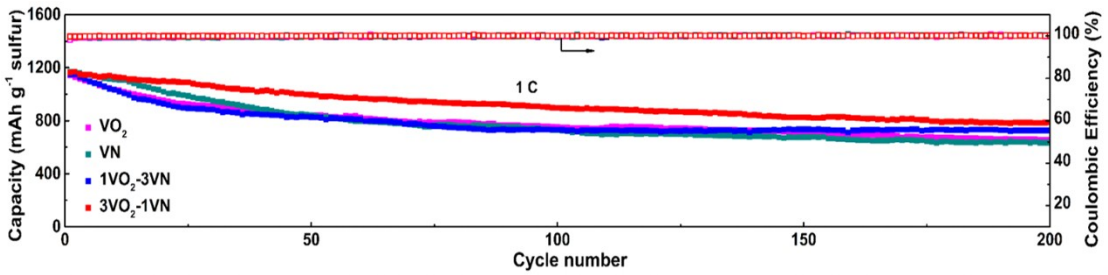

Fig. S21 Cycling performances of S@VO_2/G, S@VN/G, S@1VO_2-3VN/G, and S@3VO_2-1VN/G cathodes at 1 C.

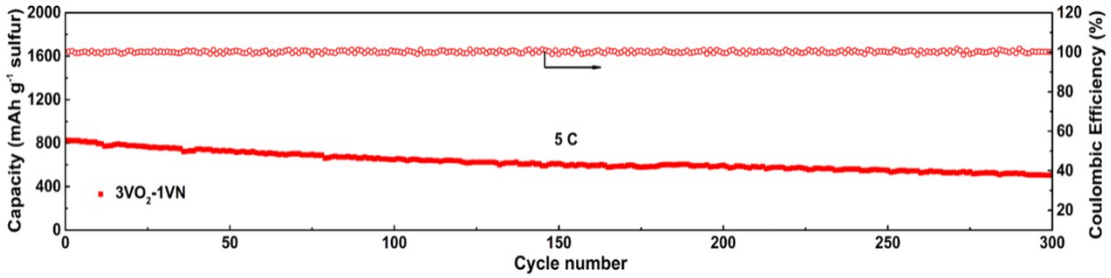

Fig. S22 Cycling performance of S@3VO_2-1VN/G cathode at 5 C.

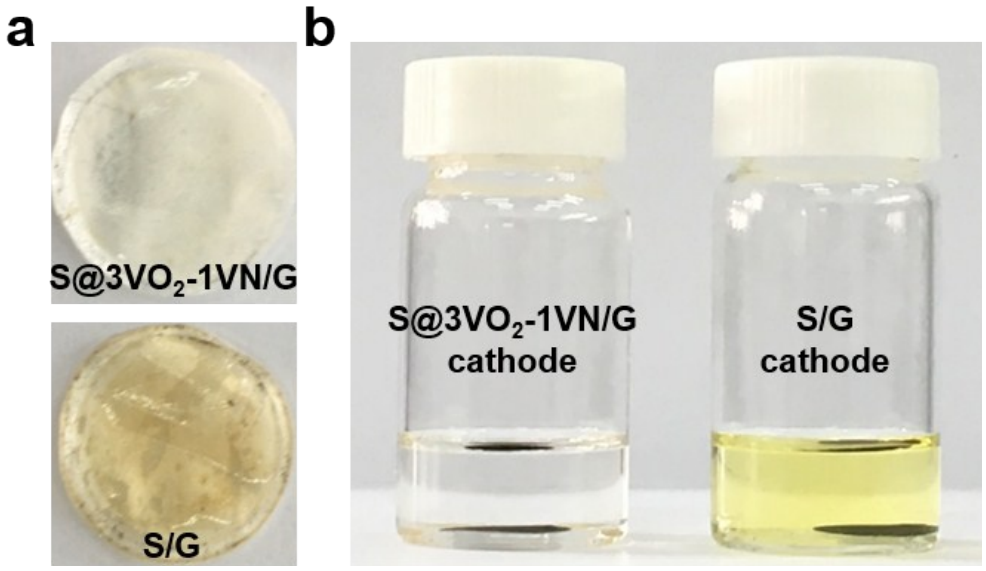

Fig. S23 Visualized test for suppressed shuttle effect. (a) Examination of the separators from disassembled batteries after 200 cycles at 1 C. (b) Examination of the S@3VO_2-VN and S@G cathodes from disassembled batteries after 200 cycles at 1 C by immersing in 5 mL DME solution for 2 h.

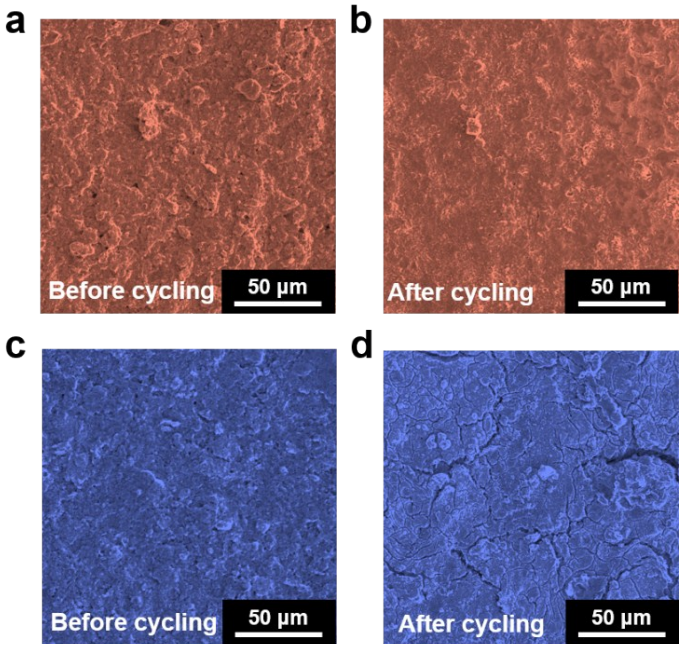

Fig. S24 SEM inspections of cathode before and after cycling. (a-b) SEM images of S@3VO_2-1VN/G cathode a) before and b) after 200 cycles at 1 C. (c-d) SEM images of bare S@G cathode c) before and d) after 200 cycles at 1 C.

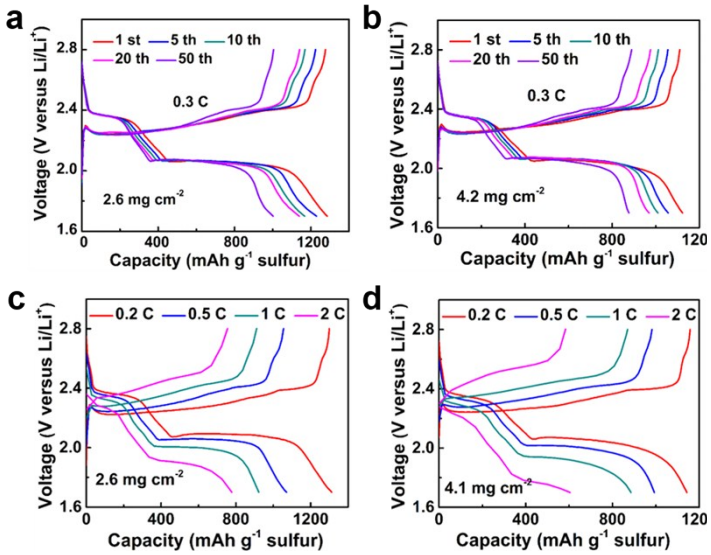

Fig. S25 Galvanostatic charge/discharge profiles of S@3VO_2-1VN/G cathodes with high sulfur loadings. (a-b) Galvanostatic charge/discharge profiles at 0.3 C with a sulfur loading of (a) 2.6 and (b) 4.2 mg cm^{-2}. (c-d) Galvanostatic charge/discharge profiles at various rates with a sulfur loading of (c) 2.6 and (d) 4.1 mg cm^{-2}.

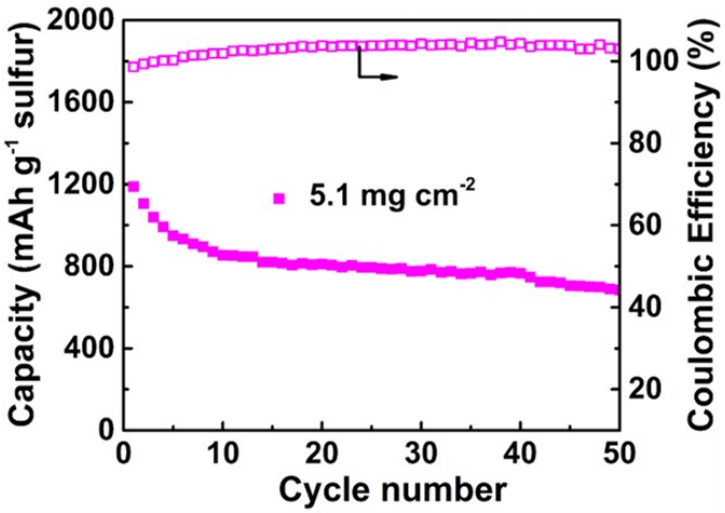

Fig. S26 Cycling performance of the S@3VO_2-1VN/G cathode at 0.1 C with a sulfur loading of 5.1 mg cm^{-2}.

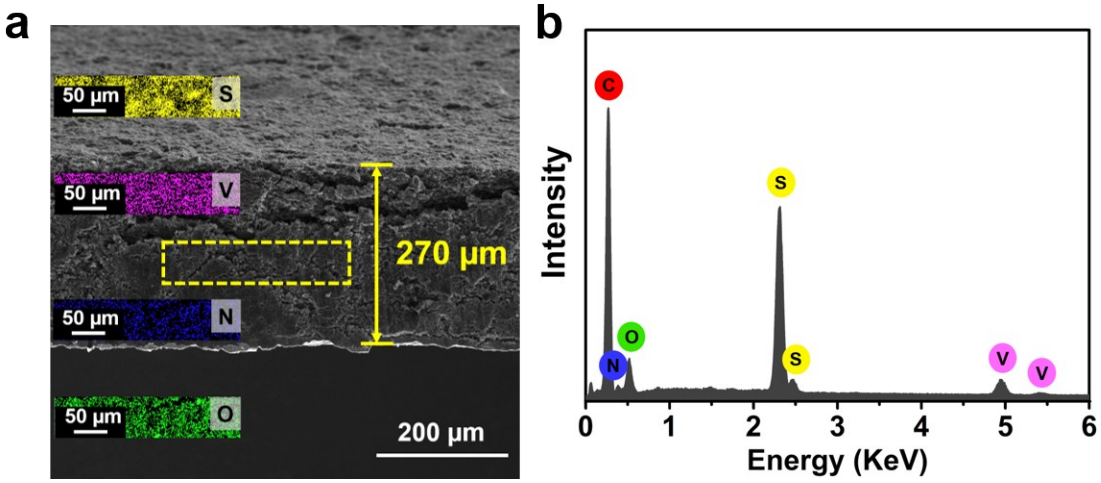

Fig. 27 SEM image and corresponding elemental characterization of S@3VO_2-1VN cathode with a sulfur mass loading of 11.4 mg cm^{-2}.

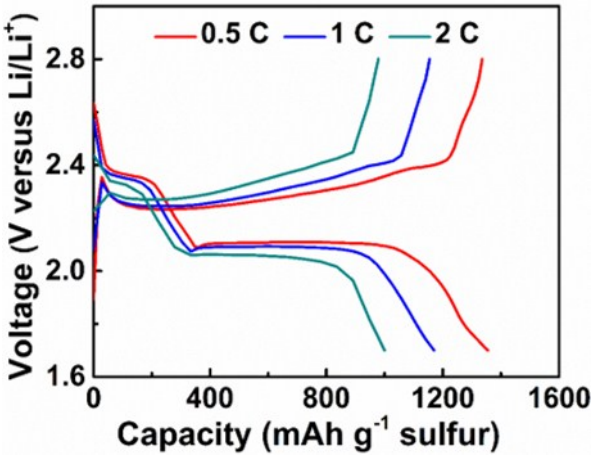

Fig. S28 Galvanostatic charge/discharge profiles of S@3VO_2-1VN/G cathode at various rates at 50°C.

Table S1 Comparation of battery performances based on sulfur hosts between this work and other reported studies.

Hosts	Mass loading of S (mg cm^{-2})	S content (wt%)	Current density (C)	Cycles	Initial capacity (mAh g^{-1})	Capacity decay (% per cycle)	Ref.
3VO_2-1VN	1.6-1.8	61.8	0.2	100	1455	0.23	This work
			2	800	1010	0.06	
	4.2	61.8	0.3	50	1125	0.44	
VS_2	1-2	61	2	100	1185	0.16	1
VO_2	1.4-2.0	56	0.2	100	1405	0.30	2
VN/C	2.8	57.2	1	200	1200	0.24	3
Co-N-GC	2.0-2.5	49	0.2	100	1440	0.40	4
MCM-Nb_2O_5	~1.5	48	2	500	1200	0.09	5
TiO_2/G	3.5	61	0.2	100	1032	0.44	6
TiC/G	3.5	61	0.2	100	1032	0.35	6
Co_3O_4	1.5-2.0	49	1	100	~ 1580	0.59	7
Co_4N	1.5-2.0	49	1	100	~1640	0.39	7
MoS_2	~1.5	60	0.5	100	1033	0.44	8

References

1. X. Zhu, W. Zhao, Y. Song, Q. Li, F. Ding, J. Sun, L. Zhang and Z. Liu, *Adv. Energy Mater.*, 2018, DOI: 10.1002/aenm.201800201.
2. Y. Song, W. Zhao, X. Zhu, L. Zhang, Q. Li, F. Ding, Z. Liu and J. Sun, *ACS Appl. Mater. & Interfaces*, 2018, **10**, 15733-15741.
3. X. Li, K. Ding, B. Gao, Q. Li, Y. Li, J. Fu, X. Zhang, P. K. Chu and K. Huo, *Nano Energy*, 2017, **40**,

655-662.

4. Y. J. Li, J. M. Fan, M. S. Zheng and Q. F. Dong, *Energy Environ. Sci.*, 2016, **9**, 1998-2004.
5. Y. Q. Tao, Y. J. Wei, Y. Liu, J. T. Wang, W. M. Qiao, L. C. Ling and D. H. Long, *Energy Environ. Sci.*, 2016, **9**, 3230-3239.
6. H. J. Peng, G. Zhang, X. Chen, Z. W. Zhang, W. T. Xu, J. Q. Huang and Q. Zhang, *Angew. Chem. Int. Ed.*, 2016, **55**, 12990-12995.
7. D. R. Deng, F. Xue, Y. J. Jia, J. C. Ye, C. D. Bai, M. S. Zheng and Q. F. Dong, *ACS Nano*, 2017, **11**, 6031-6039.
8. H. Lin, L. Yang, X. Jiang, G. Li, T. Zhang, Q. Yao, G. W. Zheng and J. Y. Lee, *Energy Environ. Sci.*, 2017, **10**, 1476-1486.